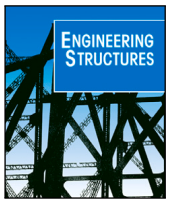
Engineering Structures 366 (2026) 123494



Contents lists available at ScienceDirect

Engineering Structures

journal homepage: www.elsevier.com/locate/engstruct



Performance evaluation of novel inerter-based vibrating barrier configurations

Predaricka Deastra [a,b,*], Hakan Dogan [c], Ruihong Xie [d], Marco Domaneschi [b]

[a] University of Brighton, School of Architecture, Technology and Engineering, Brighton, BN2 4GJ, United Kingdom
[b] Politecnico di Torino, Department of Structural, Geotechnical and Building Engineering (DISEG), Turin, 10129, Italy
[c] Hacettepe University, Department of Mechanical Engineering, Ankara, 06800, Turkey
[d] Tohoku University, International Research Institute of Disaster Science (IRIDeS), Sendai, 980-0845, Japan

ARTICLE INFO

Keywords:
Vibrating barrier
Inerter
Inerter-based vibrating barrier (IViBa)
H_∞ and H_2 optimisations
Time-domain based optimisation

ABSTRACT

A vibrating barrier is a non-invasive approach for mitigating seismic effects on buildings. Recent developments have integrated inerter-based dampers, consisting of an inerter, a spring, and a dashpot arranged in various configurations, into vibrating barriers, leading to the concept of the inerter-based vibrating barrier (IViBa). Unlike conventional applications in which inerter-based dampers are embedded within the host structure where they modify the structural dynamic properties, their use as ground-installed barriers introduces a different interaction mechanism, altering wave propagation and soil–structure interaction, and consequently leading to distinct tuning and optimisation characteristics. This study addresses this gap through an investigation of IViBa configurations and their governing parameters. To date, only one IViBa configuration has been reported. This work introduces three alternative configurations derived from different arrangements of the inerter, spring, and dashpot. The influence of secondary mass and dashpot placement is examined, with performance optimised using H_∞ and H_2 criteria implemented via the Self-Adaptive Differential Evolution algorithm and the Kanai–Tajimi filter. The results show that the newly proposed IViBa configurations with parallel inerter–dashpot configuration achieve performance comparable to the existing IViBa while requiring approximately 96% lower damping. In the time-domain simulations, the proposed time-domain optimisation yields the best structural performance for the case considered, achieving about 27% reduction in both RMS and peak responses compared to the uncontrolled case. This is followed by the H_∞ and H_2 optimisation methods, which provide average response reductions of approximately 24% and 22%, respectively. These results define a clear design framework in which optimal inertance and configuration selection govern performance, enabling efficient and practically achievable IViBa solutions for seismic response mitigation.

1. Introduction

Earthquakes have caused numerous fatalities in many seismically active regions. Inerter-based dampers have been identified in the literature as a promising technology for protecting buildings against seismic events. An inerter is a two-terminal device that generates a resisting force proportional to the relative acceleration between its terminals. The constant of proportionality between the force and acceleration difference is called the inertance, and it has units of mass (e.g., kilograms [1] or metric tons [2]). There are several mechanisms for inerter realisation that have been reported in the literature, such as mechanical geared inerter [3], fluid-based inerter [4,5], ball-screw inerter [6] and flywheel inerter [7]. A review of the physical realisation of inerters can be found in [8].

An inerter is capable of generating inertance hundreds or even thousands of times greater than its own physical mass. For instance, a mechanical geared inerter designed at the University of Cambridge [3] is capable of producing an inertance of 700 kg with a physical mass of just 3.5 kg. Similarly, a rotary inerter installed in a telecommunications building in Japan achieved an inertance of 6400 metric tons with a device mass of less than one metric ton [9]. The highest inertance-to-physical-mass ratio reported in the literature to date is approximately 1.5×10^6, attained by a hydraulic inerter developed by Nakaminami et al. [10]. This remarkable capability makes inerters particularly effective in enhancing the performance of structural control systems.

In the current body of literature, the use of inerters has been extensively explored for vibration control across a wide range of engineering systems. In the field of civil engineering, inerter-based devices have

* Corresponding author at: University of Brighton, School of Architecture, Technology and Engineering, Brighton, BN2 4GJ, United Kingdom.
E-mail address: p.deastra@brighton.ac.uk (P. Deastra).

https://doi.org/10.1016/j.engstruct.2026.123494
Received 5 January 2026; Received in revised form 18 June 2026; Accepted 30 July 2026
Available online 8 August 2026
0141-0296/© 2026 The Authors. Published by Elsevier Ltd. This is an open access article under the CC BY license (http://creativecommons.org/licenses/by/4.0/).

been successfully applied to buildings for the mitigation of seismic and wind-induced vibrations, demonstrating significant improvements in structural performance and resilience [11,12]. For wind turbines, inerters have been shown to effectively reduce structural responses arising from wind and seismic excitations, thereby enhancing operational reliability and service life [13–16]. Beyond civil structures, inerter technology has also attracted considerable attention in the aerospace sector. For example, inerters have been proposed as key components in aircraft landing gear systems to reduce impact loads during touchdown and improve shock absorption characteristics [17–19]. In manufacturing and machining applications, inerter-based devices have been investigated as a means of suppressing regenerative chatter and improving process stability and surface finish quality [20,21]. Furthermore, inerters have been incorporated into railway and automotive suspension systems, where they have demonstrated substantial potential for improving ride comfort, passenger experience, and vehicle dynamic performance [22–24].

The application of inerters for vibration control in buildings typically involves their integration with additional elements such as a spring and a dashpot. The combination of these three components is commonly referred to as an inerter-based damper [25]. Although this combination admits a wide range of possible configurations, only three archetypes have been extensively investigated in the literature: the tuned viscous mass damper (TVMD) [6], the tuned inerter damper (TID) [26], and the tuned mass damper inerter (TMDI) [27]. The effectiveness of these inerter-based dampers, both as vibration isolators and as vibration absorbers, has been widely discussed; representative studies can be found in [28–31] and the references therein. Inerter-based dampers can also be integrated into traditional tuned mass dampers (TMDs) to improve tuning effectiveness by enhancing energy dissipation and reducing mass requirements, thereby improving their performance in mitigating seismic responses [32].

The TVMD is the first inerter-based damper reported in the literature. It employs a viscous damper, a flywheel and a ball-screw mechanism that converts the translational motion resulting from the inter-story drift of the host structure into rotational motion of the flywheel [6]. Some applications of the TVMD in civil engineering can be found in [11,33–39].

The TID was first introduced by Lazar et al. [26] in 2014. It resembles a traditional TMD, except that the secondary oscillating mass, which provides inertial counterforces, is replaced by an inerter. The primary advantage of the TID over the TMD lies in its ability to achieve a significantly higher effective mass ratio with a much smaller physical mass, thanks to the presence of the inerter. Moreover, the optimal placement of the TID in multi-story buildings has been identified at the base floor [26], where the device can be installed directly on the foundation instead of being supported by beams or columns. This simplifies installation and reduces the need for structural modifications, leading to economic and practical advantages. Additionally, its positioning at the base makes it well-suited for integration with other control systems, such as base isolation. The applications of TID in base-isolated buildings have been reported in [40,41].

The TMDI was proposed by Marian et al. [27] to improve the dynamic performance of the traditional TMD while reducing its physical mass requirement. This enhancement is achieved by introducing an inerter element that connects the secondary mass to the ground or a building floor. The configuration of a TMDI is similar to that of a TID, but with the addition of a secondary mass. In other words, the TID can be regarded as a special case of the TMDI in which the secondary mass is set to zero. The inerter amplifies the inertial effect of the secondary mass, enabling comparable or improved vibration mitigation with significantly less physical mass. The application of the TMDI has been reported across various types of structures, including buildings [12,42–44], wind turbines [16,45–48], and nuclear power plants [49,50].

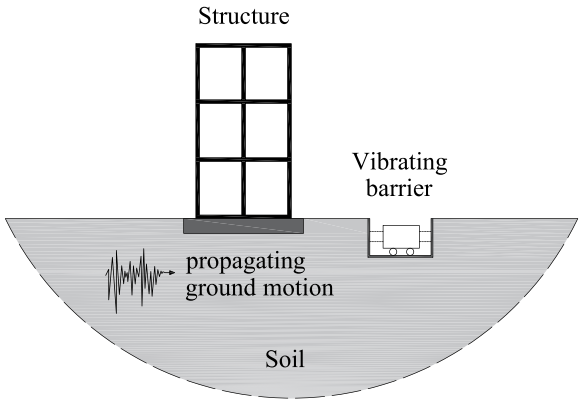


Fig. 1. Schematic depiction of a vibrating barrier used to protect an existing structure from earthquake-induced ground motion [53].

Recently, a new inerter-based damper configuration, referred to as the Novel Tuned Mass Damper Inerter (NTMDI), has been introduced in the literature [51]. This configuration was developed by modifying the placement of the spring and inerter elements in the conventional TMDI system. As a result, the NTMDI can also be regarded as a more general form of the TVMD, in which a secondary mass is included. The shake table experimental verification of this model can be found in [25,52].

Despite the promising potential of inerter-based dampers for seismic protection of buildings, their application as vibrating barriers has received limited attention. Vibrating barriers, typically buried in the ground, have been recognised in the literature as an effective solution for non-invasive earthquake protection [53]. Their unique configuration exploits soil–structure interaction (SSI) and structure–soil–structure (SSSI) interaction to attenuate seismic waves before they reach the buildings, without requiring any physical intervention to the structures themselves. It should be noted that the term "vibrating barrier" does not refer to a physical barrier that directly blocks or reflects incoming seismic waves. Instead, the device acts as a ground-coupled resonant system that interacts dynamically with the surrounding soil and the protected structure. Through SSI and SSSI mechanisms, the vibrating barrier modifies the propagation and transmission of seismic waves, leading to attenuation of the structural response. In this sense, the "barrier" effect arises from dynamic interaction rather than physical obstruction. Fig. 1 illustrates the schematic of a vibrating barrier employed for protecting a structure.

The traditional vibrating barrier adopts a TMD configuration, as first reported in [53]. Applications of this type of vibrating barrier have been documented for the protection of clusters of buildings [54], pyramidal structures [55], and historical buildings [56]. Although theoretically effective, such systems require a significantly large secondary mass to achieve a significant reduction in the response of the protected structure. Here, the secondary mass refers to the movable mass component of the vibrating barrier that provides the inertial response necessary for vibration mitigation. In conventional vibrating barrier systems, achieving significant response reduction typically requires a secondary mass on the order of the structural mass, and in some cases even larger [53]. From a practical perspective, this implies the need to mobilise or install a substantial volume of material. For example, considering typical soil densities ($\approx$1800–2000 kg/m^3), a secondary mass of 1000 tons would correspond to approximately 500–550 m^3 of soil, which poses significant challenges in terms of space requirements, construction feasibility, and cost.

In 2020, Cacciola et al. [57] addressed this limitation by incorporating an inerter into a vibrating barrier, resulting in a TMDI configuration. While inerters are often associated with lightweight advantages in conventional structural applications, this characteristic remains important in the context of vibrating barriers for a different reason. In

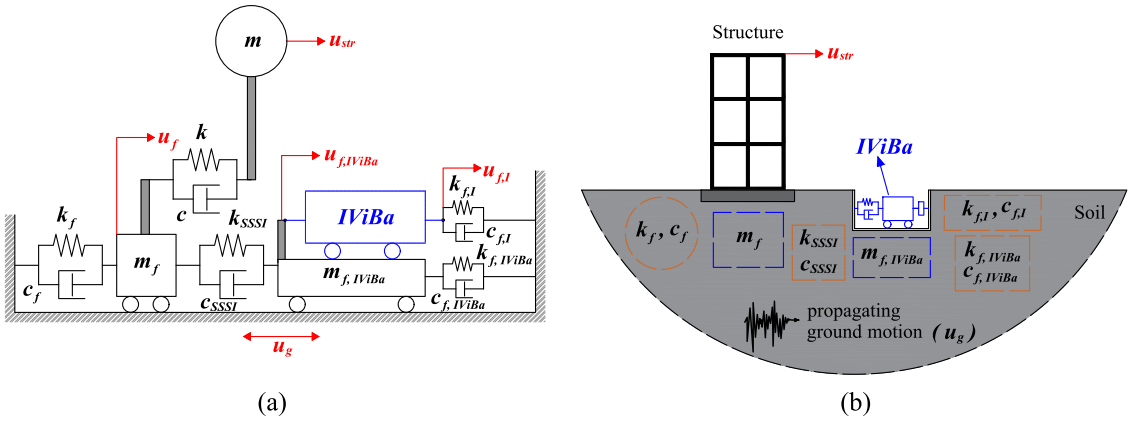


Fig. 2. Mapping of the physical system shown in Fig. 1 to its equivalent lumped-parameter model. (a) Analytical model of an SDOF structure controlled with an IViBa, and (b) Annotated physical configuration illustrating the correspondence between physical components and their lumped representations.

a traditional vibrating barrier system, achieving significant response reduction requires a secondary mass comparable to, or even exceeding, that of the protected structure [53], which is impractical due to the substantial physical space required to accommodate such a mass. The incorporation of an inerter into the vibrating barrier, as first proposed in [57], addresses this limitation by enabling large effective inertial forces without the need for excessive physical mass, thereby making the practical implementation of vibrating barriers feasible. When a vibrating barrier includes an inerter element, it is referred to as an Inerter-Based Vibrating Barrier (IViBa). To date, the TMDI configuration remains the only inerter-based damper that has been investigated specifically for use as a vibrating barrier.

This paper examines three alternative inerter-based damper configurations for use as vibrating barriers and compares their performance with that of the existing IViBa system, which adopts a TMDI configuration. The proposed layouts are derived from the TID, TVMD, and NTMDI systems. Although these configurations have been extensively studied in the literature as vibration control devices when directly attached to host structures, their dynamic behaviour when deployed as vibrating barriers is fundamentally different and has not yet been investigated.

This work provides the first systematic investigation of how inerter-based damper configurations, originally conceived for direct structural attachment, perform when repurposed as ground-installed vibrating barriers. Unlike conventional inerter-based dampers, IViBa systems interact with the soil–structure system through complex SSI and SSSI mechanisms, leading to fundamentally different dynamic characteristics and optimisation requirements. The study demonstrates that IViBa systems exhibit an optimal inertance beyond which performance no longer improves, a behaviour not observed in traditional inerter-based vibration control devices. Furthermore, the influence of dashpot placement and secondary mass inclusion is quantified, revealing clear trade-offs between stiffness demand, damping demand, and achievable response reduction. These findings provide practical design-oriented insight and establish a rational basis for selecting IViBa configurations under realistic engineering constraints.

The remainder of this paper is organised as follows. Section 2 presents the governing equations and transfer functions of the IViBa configurations. Sections 3 and 4 describe the H_∞ and H_2 optimisation approaches, respectively, for evaluating the performance of the four IViBa configurations in protecting an SDOF structure. Section 5 discusses the performance of the IViBa systems in the time domain. Finally, conclusions are drawn in Section 6.

2. Governing equations and transfer functions

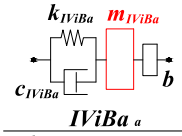
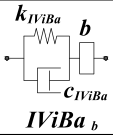
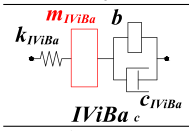
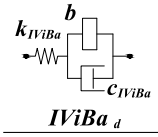
The analytical model of a single story structure controlled by an IViBa is illustrated in Fig. 2(a), adopted from Cacciola, et al. [57]. The structure is simplified by a lumped mass model consisting of a mass m supported by a parallel spring-dashpot representing the column stiffness k and structural viscous damping coefficient c, respectively. The compliant soil layer supporting the structure is modelled as a mass m_f with the SSI effects captured using soil stiffness k_f and damping coefficient c_f. The structure is protected by an IViBa housed within a containment mass $m_{f,IViBa}$. The influence of SSSI is modelled using a spring and dashpot characterised by stiffness k_{SSSI} and damping coefficient c_{SSSI}. The SSI effects related to this containment are modelled using spring stiffness $k_{f,IViBa}$ and damping $c_{f,IViBa}$. Further, $k_{f,I}$ and $c_{f,I}$ represent the stiffness and damping coefficient of the soil compliance at the connection of the IViBa to the ground. Fig. 2(b) shows the mapping of the physical system shown in Fig. 1 to its equivalent lumped-parameter model in Fig. 2(a).

It is worth noting that, although the analytical model illustrated in Fig. 2(a) is a simplified representation of a more complex physical system shown in Fig. 2(b), previous studies, such as those by Cacciola and Tombari [53] and Tombari et al. [54], have demonstrated that this modelling approach delivers sufficiently accurate results for vibrating barrier design. These findings were supported through validation against advanced finite element and boundary element simulations. The performance of IViBa systems may also be influenced by the presence of nearby structures through SSSI effects. While such interactions are represented in a simplified form in the present model, more complex scenarios involving multiple adjacent structures may alter the dynamic response and optimal tuning parameters of the system. A detailed investigation of these effects is beyond the scope of this study and is left for future work.

The new IViBa configurations proposed in this study, namely IViBa$_b$, IViBa$_c$, and IViBa$_d$, are illustrated in Fig. 3(b)–(d). Their performance is compared with that of IViBa$_a$ depicted in Fig. 3(a), which is the only IViBa configuration previously examined in the literature [57]. Each IViBa configuration consists of a spring with stiffness k_{IViBa}, a dashpot with viscous damping coefficient c_{IViBa}, and an inerter with inertance b. In addition, IViBa$_a$ and IViBa$_c$ include a secondary mass, m_{IViBa}, which is often referred to in the literature as the mass of the device, connection, or any intentionally added mass [25].

As previously mentioned, the four IViBa configurations considered in this paper, when attached directly to a structure, are referred to as inerter-based dampers and have been extensively studied in the literature. However, their application as vibration barriers has received limited attention; to date, IViBa$_a$ is the only configuration reported in

Table 1
Comparison of IViBa configurations and their equivalent classical inerter-based devices when attached directly to a host structure.

Configurations	Key components and arrangement	Equivalent device (direct attachment to host structure)
	Spring (k_{IViBa}), dashpot (c_{IViBa}), secondary mass (m_{IViBa}) and inerter (b). The spring is connected in parallel with the dashpot, and this parallel combination is connected in series with the secondary mass and the inerter. This is currently the only IViBa configuration reported in the literature [57].	Known as the TMDI, it was first proposed by Marian et al. [27]. The concept involves attaching an inerter as an additional element to a traditional TMD to reduce the required physical mass.
	Spring (k_{IViBa}), dashpot (c_{IViBa}) and inerter (b). This configuration can also be considered as a special case of IViBa$_a$ when $m_{IViBa} = 0$.	Known as the TID, it was first proposed by Lazar et al. [26]. The concept replaces the mass of a traditional TMD with an inerter to reduce the required physical mass.
	Inerter (b), dashpot (c_{IViBa}), secondary mass (m_{IViBa}) and spring (k_{IViBa}). The IViBa$_c$ configuration is proposed in this paper by repositioning the dashpot in IViBa$_a$ so that it is in parallel with the inerter.	Known as the NTMDI, it was first proposed by Li et al. [51]. Its realisation was subsequently introduced in [25] and tested in a shake table experiment.
	Spring (k_{IViBa}), dashpot (c_{IViBa}) and inerter (b). This configuration can also be considered as the special case of IViBa$_c$ when $m_{IViBa} = 0$.	Known as the TVMD, this configuration was the first inerter-based damper proposed in the literature by Ikago et al. [6]. The parallel-connected inerter and dashpot are often designed as a single device; see [6,25].

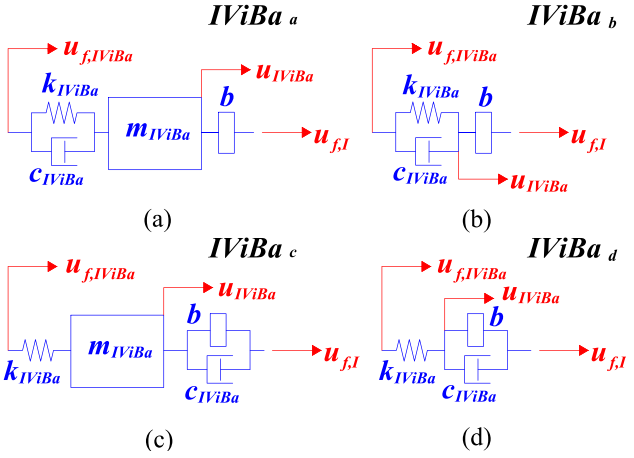


Fig. 3. IViBa configurations: (a) IViBa$_a$, (b) IViBa$_b$, (c) IViBa$_c$, and (d) IViBa$_d$.

this context [57]. Table 1 presents a comparison of the IViBa configurations and their equivalent classical inerter-based devices when attached directly to a host structure.

As shown in Fig. 3(a)–(d) and Table 1, all IViBa configurations exhibit similar overall layouts. The primary distinction lies in the position of the dashpot and the presence of a secondary mass, m_{IViBa}. In the following two subsections, we present the equations of motion for the parallel-connected spring-dashpot and the parallel-connected inerter-dashpot systems, which serve as the fundamental components of these configurations.

2.1. Parallel spring-dashpot configurations (ViBa$_a$ and IViBa$_b$)

The equation of motion of the system shown in Fig. 2(a) with IViBa$_a$ and IViBa$_b$ in relative coordinate system can be written as

$$\mathbf{M}_{a,b}\ddot{\mathbf{u}}(t) + \mathbf{C}_{a,b}\dot{\mathbf{u}}(t) + \mathbf{K}_{a,b}\mathbf{u}(t) = -\bar{\mathbf{M}}_{a,b}\ddot{u}_g(t) \tag{1}$$

where $\mathbf{M}_{a,b}, \mathbf{C}_{a,b}, \mathbf{K}_{a,b}$ and $\bar{\mathbf{M}}_{a,b}$ matrices are given as follows:

$$\mathbf{M}_{a,b} = \begin{bmatrix} m_f & 0 & 0 & 0 & 0 \\ 0 & m & 0 & 0 & 0 \\ 0 & 0 & m_{f,IViBa} & 0 & 0 \\ 0 & 0 & 0 & b + m_{IViBa} & -b \\ 0 & 0 & 0 & -b & b \end{bmatrix}$$

$$\mathbf{C}_{a,b} = \begin{bmatrix} c_f + c_{SSSI} + c & -c & -c_{SSSI} & 0 & 0 \\ -c & c & 0 & 0 & 0 \\ -c_{SSSI} & 0 & c_{SSSI} + c_{f,IViBa} + c_{IViBa} & -c_{IViBa} & 0 \\ 0 & 0 & -c_{IViBa} & c_{IViBa} & 0 \\ 0 & 0 & 0 & 0 & c_{f,I} \end{bmatrix}$$

$$\mathbf{K}_{a,b} = \begin{bmatrix} k_f + k_{SSSI} + k & -k & -k_{SSSI} & 0 & 0 \\ -k & k & 0 & 0 & 0 \\ -k_{SSSI} & 0 & k_{SSSI} + k_{f,IViBa} + k_{IViBa} & -k_{IViBa} & 0 \\ 0 & 0 & -k_{IViBa} & k_{IViBa} & 0 \\ 0 & 0 & 0 & 0 & k_{f,I} \end{bmatrix};$$

$$\bar{\mathbf{M}}_{a,b} = \begin{bmatrix} m_f \\ m \\ m_{f,IViBa} \\ m_{IViBa} \\ 0 \end{bmatrix}$$

It should be noted that for the IViBa$_b$ the secondary mass m_{IViBa} should be set to zero. The transfer function of the system in the Laplace domain can be written as:

$$T(s) = \frac{\mathbf{U}_{a,b}(s)}{U_g(s)} = (\mathbf{M}_{a,b}s^2 + \mathbf{C}_{a,b}s + \mathbf{K}_{a,b})^{-1}(-\bar{\mathbf{M}}_{a,b}s^2) \tag{2}$$

where s denotes the Laplace transform variable, defined as $s = i\omega$, with ω representing the angular frequency of the ground displacement input $u_g(t)$, and $i = \sqrt{-1}$. $\mathbf{U}_{a,b}(s)$ is the matrix of the displacement response in the Laplace domain, expressed as:

$$\mathbf{U}_{a,b}(s) = [U_f \quad U_{str} \quad U_{f,IViBa} \quad U_{IViBa} \quad U_{f,I}]^T \tag{3}$$

2.2. Parallel inerter-dashpot configurations (IViBa$_c$ and IViBa$_d$)

Similar to the previous case, the equation of motion of the system shown in Fig. 2(a) with IViBa$_c$ and IViBa$_d$ in relative coordinate system

Table 2
Parameters for the model shown in Fig. 2(a) adopted from [57].

Parameters	SDOF structure	SSI (structure)	SSI (IViBa)	SSSI	Inerter
Mass (kg)	$m = 0.59$	$m_f = 0.353$	$m_{f,IViBa} = 0.491$	–	$m_{f,I} = 0$
Stiffness (N/m)	$k = 909.85$	$k_f = 640$	$k_{f,IViBa} = 760$	$k_{SSSI} = 315$	$k_{f,I} = 760$
Damping coefficient (N s/m)	$c = 4.0$	$c_f = 2.81$	$c_{f,IViBa} = 3.34$	$c_{SSSI} = 0.28$	$c_{f,I} = 3.34$

can be written as

$$\mathbf{M}_{c,d}\ddot{\mathbf{u}}(t) + \mathbf{C}_{c,d}\dot{\mathbf{u}}(t) + \mathbf{K}_{c,d}\mathbf{u}(t) = -\bar{\mathbf{M}}_{c,d}\ddot{u}_g(t) \tag{4}$$

where $\mathbf{C}_{c,d}$ matrix is given as follows:

$$\mathbf{C}_{c,d} = \begin{bmatrix} c_f + c_{SSSI} + c & -c & -c_{SSSI} & 0 & 0 \\ -c & c & 0 & 0 & 0 \\ -c_{SSSI} & 0 & c_{SSSI} + c_{f,IViBa} & 0 & 0 \\ 0 & 0 & 0 & c_{IViBa} & -c_{IViBa} \\ 0 & 0 & 0 & -c_{IViBa} & c_{IViBa} + c_{f,I} \end{bmatrix}$$

The matrices $\mathbf{K}_{c,d}$ and $\bar{\mathbf{M}}_{c,d}$ are identical to $\mathbf{K}_{a,b}$ and $\bar{\mathbf{M}}_{a,b}$, respectively. As in IViBa$_b$, the secondary mass m_{IViBa} in IViBa$_d$ should be set to zero. Accordingly, the transfer function of the system in the Laplace domain is expressed as:

$$T(s) = \frac{\mathbf{U}_{c,d}(s)}{U_g(s)} = (\mathbf{M}_{c,d}s^2 + \mathbf{C}_{c,d}s + \mathbf{K}_{c,d})^{-1}(-\bar{\mathbf{M}}_{c,d}s^2) \tag{5}$$

$\mathbf{U}_{c,d}(s)$ is the matrix of the displacement response in the Laplace domain, which is the same as $\mathbf{U}_{a,b}(s)$ in Eq. (3).

Next, two optimisation strategies are employed to optimise the performance of the IViBa systems. The H_∞ optimisation is used to determine the optimal design parameters by minimising the peak structural response in the frequency domain, thereby representing a worst-case scenario. In contrast, the H_2 optimisation evaluates the mean energy response under stochastic seismic excitation based on the Kanai–Tajimi spectrum [58,59]. These approaches are complementary, providing insight into both peak response control and overall seismic performance.

3. H_∞ optimisation for harmonic base excitation

In H_∞ optimisation, the objective is to minimise the peak structural response in the frequency domain. In this study, the optimisation is performed using the SaDE algorithm [60], implemented in MATLAB. SaDE is an enhanced variant of Differential Evolution in which control parameters and mutation strategies are adaptively updated based on their historical performance. Multiple mutation strategies compete during the search process, and their selection probabilities are adjusted to favour those yielding improved solutions [60]. This adaptive mechanism reduces the need for manual parameter tuning and improves robustness in solving the nonlinear optimisation problems considered herein.

It should be noted that closed-form analytical solutions based on fixed-point theory can be, in principle, derived for the optimisation problem in this study. However, fixed-point theory is strictly valid for undamped systems, where invariant intersection points can be identified in the transmissibility response. However, in the presence of multiple non-zero damping components in the system shown in Fig. 2(a), these invariant points no longer exist. Consequently, analytical tuning strategies based on fixed-point formulations are not directly applicable, motivating the use of numerical optimisation in this study.

In this study, the parameters of the analytical model shown in Fig. 2(a) are adopted from the physical properties of a small-scale prototype reported in [53]. These parameters were also used in [57] to evaluate the performance of IViBa$_a$, which remains the only configuration reported in the literature to date. To enable a consistent and meaningful comparison between the proposed IViBa configurations and the existing one, the same set of structural parameters is adopted here and summarised in Table 2.

Table 3
Optimal parameters for IViBa configurations without a secondary mass (IViBa$_b$ and IViBa$_d$).

μ	IViBa$_b$		IViBa$_d$	
	k_{IViBa} (N/m)	c_{IViBa} (N s/m)	k_{IViBa} (N/m)	c_{IViBa} (N s/m)
$\gamma = 0$				
0.50	339.22	4.21	390.01	1.17
0.75	745.17	21.02	1258.51	1.96
0.85	898.45	41.16	2634.23	2.31
0.90	822.46	56.74	4816.67	2.46
0.95	557.59	73.64	19 644.53	2.69
0.97	–	–	$\mathbf{5.16 \times 10^{11}}$	**2.60**
1.00	27.45	79.97	8.69×10^{12}	2.10
1.002	**10.72**	**81.83**	–	–
1.10	0.00	77.20	9.63×10^{12}	3.04
1.15	0.00	68.28	9.97×10^{12}	3.43
1.25	0.00	60.14	8.75×10^{13}	4.22

A recent study [25] demonstrated that the transfer function from ground displacement to floor displacement relative to the ground is particularly useful for assessing device performance in terms of damping, as the inverse of its peak value provides an approximation of twice the damping ratio of the corresponding mode. Motivated by this insight, the optimisation problem in this work is formulated by tuning the stiffness and damping parameters to minimise the H_∞ norm of the transfer function from ground displacement to floor displacement relative to the ground, defined as:

$$\min\left(\max\left|\frac{U_{\text{str}}(s)}{U_g(s)}\right|\right). \tag{6}$$

To compare the performance of the four IViBa systems based on their fundamental layout differences as presented in Table 1, this section is divided into two subsections. Section 3.1 examines the effect of the dashpot position by comparing IViBa$_b$ with IViBa$_d$, and IViBa$_a$ with IViBa$_c$, where a secondary mass is present in the latter pair. Section 3.2 investigates the influence of the secondary mass by comparing the performance of IViBa$_a$ and IViBa$_b$, as well as IViBa$_c$ and IViBa$_d$.

3.1. The effect of the dashpot position

This subsection evaluates the effect of the dashpot position in the IViBa configurations. In IViBa$_a$ and IViBa$_b$, the dashpot is connected in parallel with the spring, while in IViBa$_c$ and IViBa$_d$ it is positioned in parallel with the inerter. To quantify the influence of this configuration change, the optimal parameters are obtained through the H_∞ optimisation framework described in the previous section. The corresponding optimal IViBa parameters for different inertance ratios $\mu = b/m$ are presented in Table 3 for configurations without a secondary mass and Table 4 for configurations with a secondary mass.

Figs. 4(a) and 4(b) present the frequency responses of the structure equipped with the optimal IViBa systems without the secondary mass ($\gamma = 0$, where $\gamma = m_{IViBa}/m$), namely IViBa$_b$ and IViBa$_d$, illustrating the influence of increasing inertance on the dynamic behaviour. The inertance is expressed in non-dimensional form as the inertance ratio μ. As listed in Table 3, the values of μ are varied from 0.5 to 1.25. It is worth noting that realising such high inertance values is feasible in practice as inerters can achieve large inertance with small physical mass using mechanisms such as ball-screw, gear, or fluid flow systems [8]. Both figures demonstrate that the optimal frequency responses exhibit two

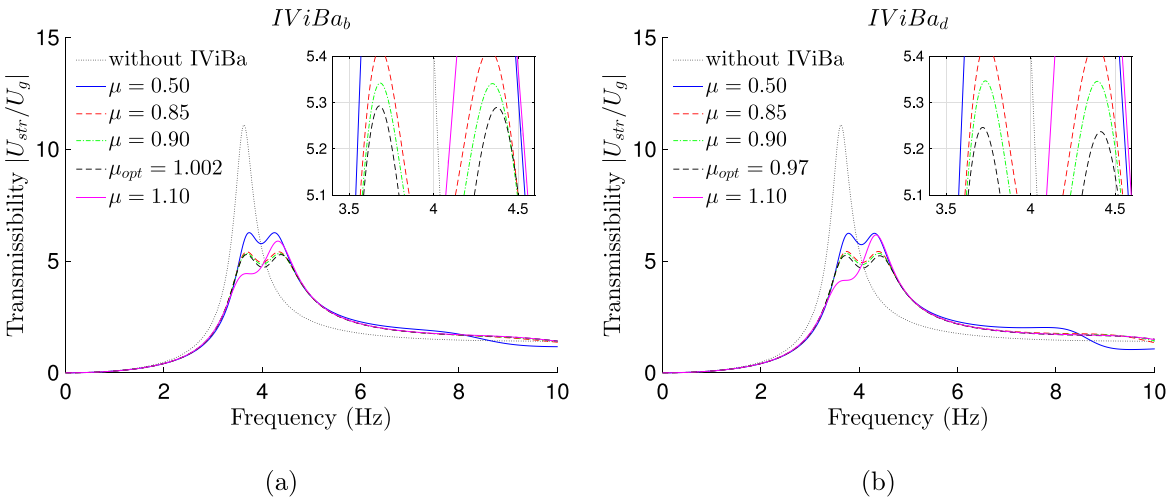


Fig. 4. Performance comparison between IViBa$_b$ and IViBa$_d$.

equal peaks, analogous to those observed in traditional vibration absorbers. Increasing μ generally leads to a reduction in the response amplitude; however, this trend is observed only up to an optimal value μ_{opt} (highlighted in bold in Table 3). For the cases considered, μ_{opt} is found to be approximately 1.002 and 0.97, respectively, at which the minimum peak response is achieved. Beyond these values, further increases in μ do not lead to additional improvement and instead result in a deterioration of performance due to the loss of the equal-peak condition.

Importantly, this finding reveals that a distinct optimal inertance exists when inerter-based dampers are implemented as vibrating barriers, a behaviour not observed when such devices are directly attached to the primary structure. This highlights a fundamental difference in the dynamic characteristics of IViBa systems and underscores the critical role of inertance tuning in their optimal performance. This optimal inertance value can be identified through the simultaneous optimisation of the three parameters: b, k_{IViBa} and c_{IViBa}. A similar observation of an optimal inertance has also been reported for the system considered in [29]; however, that study does not consider a base-excited configuration, and therefore the underlying dynamics and optimality conditions differ from those investigated here.

The existence of an optimal inertance can be interpreted from the dual role of the inerter. When the inertance is relatively small, the inertial forces generated by the device are insufficient to significantly modify the dynamic response of the system. As the inertance increases, the inerter becomes increasingly effective and the structural response is reduced. However, further increases in inertance progressively suppress the relative motion across the inerter, particularly in configurations where the inerter is connected in series with a spring element. Consequently, the device deformation required to mobilise the inerter force is reduced, limiting the effectiveness of additional inertance. The competition between increasing inertial force generation and decreasing device deformation therefore gives rise to an optimal inertance beyond which no further performance improvement is obtained.

Furthermore, as shown in Table 3, The corresponding optimal stiffness k_{IViBa} and damping coefficient c_{IViBa} vary significantly with μ. For IViBa$_b$, both parameters increase with μ up to values close to μ_{opt}, beyond which they decrease. In contrast, for IViBa$_d$, the optimal stiffness increases rapidly with μ, reaching unrealistically large values as μ approaches μ_{opt}, while the optimal damping coefficient remains relatively low. Determining the optimal inertance is therefore crucial, as values close to or beyond this point may lead to physically unrealistic optimal stiffness, which approaches zero for IViBa$_b$ and grows excessively for IViBa$_d$.

The rapid increase in the optimal stiffness of IViBa$_d$ can be interpreted by noting that, at large inertance values, the inerter introduces dominant acceleration-dependent forces, effectively constraining relative motion and leading to a stiffness-dominated response. In the vicinity of the optimal inertance, the H_∞ optimisation increases the stiffness to balance these inertial forces and maintain a near equal-peak condition. This behaviour is consistent with the known characteristics of inerter-based systems with parallel inerter–dashpot configurations, where, for sufficiently large inertial effects ($b\omega^2 \gg k$), the response approaches a stiff coupling [52]. This mechanism explains why the stiffness increases to counterbalance the growing inertial forces.

It should be emphasised that the H_∞ optimisation presented herein is intentionally unconstrained and is primarily intended to investigate the fundamental dynamic behaviour and performance limits of the different IViBa configurations. For practical implementation, realistic constraints on the design parameters are required. This aspect is addressed in Section 5, where explicit bounds are imposed on the optimisation variables to obtain physically realisable solutions suitable for engineering applications.

Next, a comparison is conducted between IViBa$_a$ and IViBa$_c$, which have configurations analogous to IViBa$_b$ and IViBa$_d$, respectively, but incorporate a secondary mass m_{IViBa} expressed in non-dimensional form as the secondary mass ratio γ. Simulations are performed for $\gamma = 0.25$ and 0.5. These values are selected to reflect practical design conditions, as larger values of γ would result in excessively large secondary masses, requiring substantial installation space and significant soil excavation for IViBa implementation. The inertance ratios μ is varied from 0.5 to 1.0. The corresponding optimal parameters are summarised in Table 4. The values in bold correspond to the optimal inertance ratio, μ_{opt}.

Figs. 5(a) and 5(b) present the frequency responses of the structure equipped with IViBa$_a$ and IViBa$_c$, respectively, for $\gamma = 0.25$. As observed from these figures, the optimisation results in two equal peaks, representing the minimum achievable response for a given μ and γ. Likewise, Figs. 5(c) and 5(d) show the frequency responses of the structure equipped with IViBa$_a$ and IViBa$_c$, respectively, for $\gamma = 0.5$. A similar behaviour is observed, where the optimisation produces two equal peaks, and increasing μ further reduces the peak response until it reaches an optimal value μ_{opt}.

Similar to the previously discussed configurations, an optimal inertance also exists in these cases, representing the maximum inertance that yields the lowest possible peak response. However, unlike in IViBa$_b$ and IViBa$_d$, in IViBa$_a$ and IViBa$_c$, it is still possible to achieve two equal peaks response for b larger than b_{opt}. For example, as shown in Fig. 5(d),

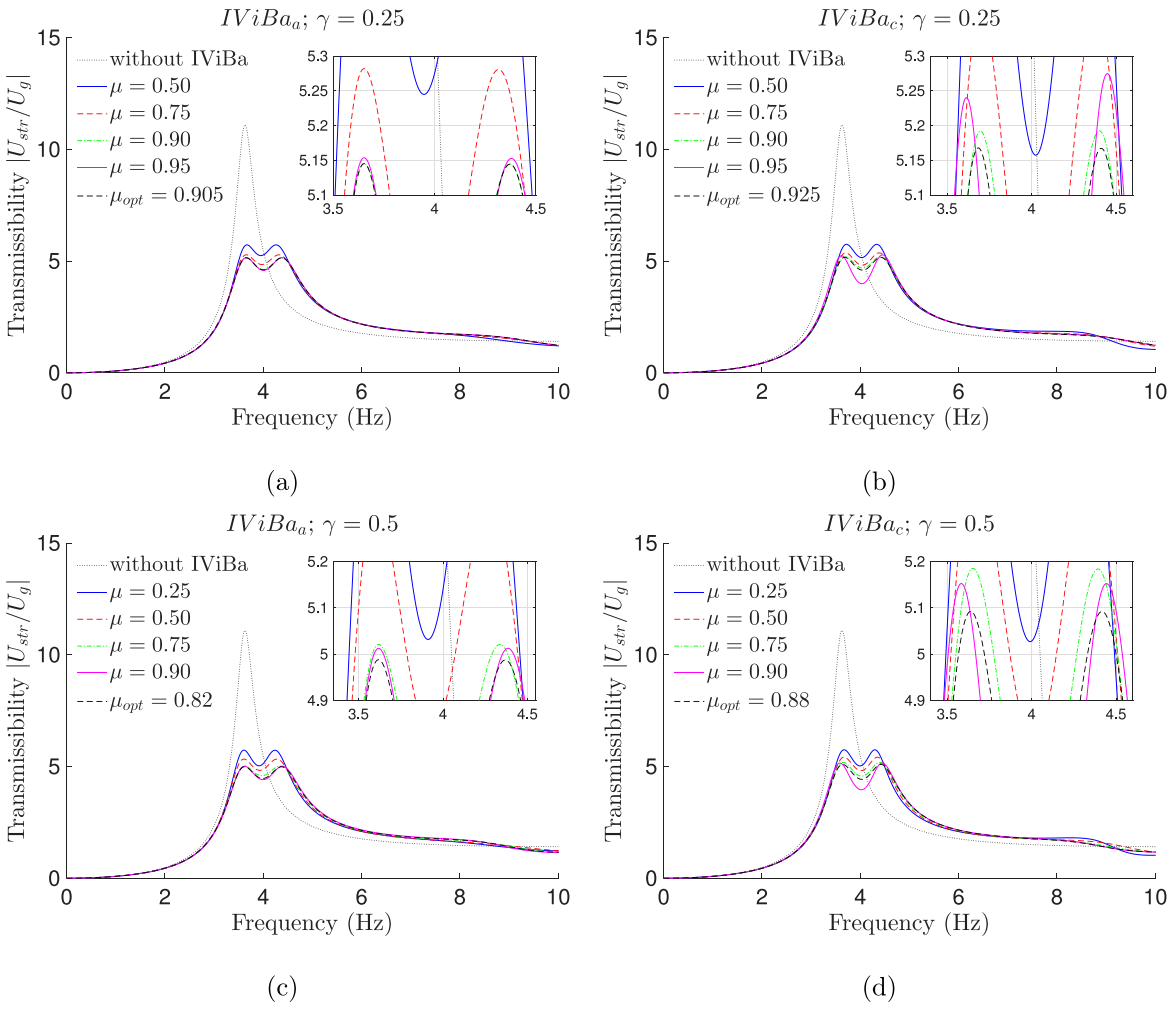


Fig. 5. Performance comparison between IViBa$_a$ and IViBa$_c$: (a, b) correspond to $\gamma = 0.25$, while (c, d) correspond to $\gamma = 0.5$.

the response at $\mu = 0.90$ is higher than the response at $\mu = 0.88$ which is the μ_{opt}.

Furthermore, as shown in Table 4, IViBa$_a$ is characterised by a lower optimal stiffness requirement k_{IViBa}, while IViBa$_c$ achieves comparable performance with a substantially reduced optimal damping coefficient c_{IViBa}. For IViBa$_a$, the optimal stiffness k_{IViBa} increases with increasing μ. This trend remains consistent up to a certain range, namely for $0.80 \leq \mu \leq 0.85$ when $\gamma = 0.25$, and for $0.75 \leq \mu \leq 0.85$ when $\gamma = 0.5$. Beyond these ranges, the optimal k_{IViBa} begins to decrease. For IViBa$_c$, the optimal stiffness k_{IViBa} increases at an even higher rate as μ increases, until it reaches a critical range. Specifically, this occurs for $0.92 \leq \mu \leq 0.93$ when $\gamma = 0.25$, and for $0.85 \leq \mu \leq 0.90$ when $\gamma = 0.5$. Beyond these values, the optimal k_{IViBa} becomes unrealistically large.

It is important to note that the newly proposed configurations, IViBa$_c$ and IViBa$_d$ achieve performance comparable to that of IViBa$_a$ and IViBa$_b$. Notably, in the vicinity of the optimal inertance, IViBa$_c$ and IViBa$_d$ require approximately 96% lower damping coefficients than IViBa$_a$ and IViBa$_b$, highlighting a significant reduction in damping demand while maintaining similar levels of response mitigation. This is particularly advantageous from a practical perspective, as achieving high levels of damping is often more challenging than providing equivalent stiffness in real-world implementations.

The influence of device topology can be understood from the different dynamic interactions among the inerter, spring, and dashpot elements. In configurations with a parallel inerter-dashpot arrangement, part of the vibration mitigation is achieved through inertia-induced force transmission, reducing the reliance on viscous energy dissipation and therefore lowering the required damping coefficient. In contrast, configurations with a parallel spring-dashpot arrangement rely more heavily on viscous dissipation to achieve response reduction. This interpretation is consistent with the high-frequency asymptotic behaviour previously reported for inerter-based devices [52], where different topologies converge to distinct equivalent dynamic configurations when inertial effects become dominant. Consequently, comparable levels of vibration mitigation can be achieved through different combinations of stiffness, damping, and inertance, highlighting the important role of device topology in determining the optimal design parameters.

In conclusion, three new configurations can be derived by altering the position of the dashpot and removing the secondary mass element from IViBa$_a$, which is currently the only IViBa configuration available in the literature. These new configurations are capable of achieving a comparable level of performance to that of the existing IViBa$_a$. When the dashpot is positioned in parallel with the inerter, the system benefits from a lower required optimal damping coefficient c_{IViBa}; however, the corresponding optimal stiffness k_{IViBa} becomes significantly larger, reaching unrealistic values as μ approaches μ_{opt}. These extreme stiffness requirements should not be interpreted as realisable design targets, but rather as indicators that the system response becomes increasingly

Table 4
Optimal parameters for IViBa configurations with a secondary mass (IViBa$_a$ and IViBa$_c$).

μ	IViBa$_a$		IViBa$_c$	
	k_{IViBa} (N/m)	c_{IViBa} (N s/m)	k_{IViBa} (N/m)	c_{IViBa} (N s/m)
$\gamma = 0.25$				
0.50	501.96	8.52	620.91	1.72
0.75	888.96	35.15	2006.10	2.44
0.80	900.78	47.17	2972.61	2.61
0.85	802.41	61.91	5300.21	2.79
0.90	514.57	76.50	17 848.18	2.93
0.905	**470.34**	**77.80**	–	–
0.92	339.25	80.78	300 274.80	3.04
0.925	–	–	$\mathbf{6.99 \times 10^{11}}$	**2.89**
0.93	241.82	82.30	6.55×10^{10}	2.69
0.94	140.15	83.36	9.40×10^{10}	2.32
0.95	36.31	83.91	9.76×10^{10}	2.05
1.00	0.00	89.74	8.77×10^{10}	2.48
$\gamma = 0.50$				
0.25	385.74	4.92	438.55	1.69
0.50	684.74	15.30	942.51	2.33
0.75	893.46	54.78	3432.08	2.89
0.82	**631.17**	**76.17**	–	–
0.85	485.87	82.78	19 119.99	3.16
0.88	–	–	$\mathbf{1.00 \times 10^{7}}$	**3.09**
0.90	1.76	88.17	2.02×10^{16}	2.52
0.92	0.00	112.19	4.96×10^{15}	2.22
0.93	0.00	103.84	2.64×10^{16}	2.46
0.94	0.00	108.12	6.04×10^{16}	2.41
1.00	0.00	94.34	2.61×10^{16}	2.72

stiffness-dominated. Consequently, achieving effective and physically meaningful IViBa designs necessitates the simultaneous optimisation of inertance b, stiffness k_{IViBa}, and damping c_{IViBa}.

It should be noted that a detailed comparison between conventional vibrating barrier without inerter element (TMD configuration) and IViBa is beyond the scope of the present study, as this has been comprehensively addressed in [57]. The present work focuses on the comparative assessment of different IViBa configurations. The differences in performance among the considered configurations arise from the way the inerter interacts with the spring and dashpot elements. Unlike the dashpot, which provides energy dissipation, the inerter generates forces proportional to relative acceleration, thereby modifying the effective inertia of the system. In configurations where the inerter is arranged in parallel with the dashpot, part of the vibration mitigation is achieved through inertia-induced force transmission rather than viscous dissipation alone. As a result, comparable response reduction can be achieved with lower optimal damping coefficients. In contrast, configurations with a parallel spring–dashpot arrangement rely more directly on viscous dissipation, leading to higher damping demand.

It should be emphasised that the objective of the proposed configurations is not solely to achieve greater response reduction than the reference IViBa$_a$ system. Rather, the aim is to explore alternative inerter-based layouts that offer different design trade-offs while maintaining comparable vibration mitigation performance. The results demonstrate that the arrangement of the inerter, spring, dashpot, and secondary mass has a significant influence on the required design parameters. Consequently, the proposed configurations expand the available design space for IViBa systems and provide additional flexibility for practical implementation under different engineering constraints.

3.2. The effect of the secondary mass

Another key distinction among the four IViBa configurations is the presence or absence of the secondary mass element, m_{IViBa}, as shown in Fig. 3(a)–(d). Specifically, IViBa$_a$ and IViBa$_b$ share an identical spring-dashpot parallel layout; however, only IViBa$_a$ incorporates the

Table 5
Optimal parameters for IViBa$_a$ and IViBa$_b$ (parallel spring-dashpot configurations) for total mass ratios ($\mu + \gamma$) of 0.75 and 1.00.

γ	μ	IViBa$_a$		IViBa$_b$	
		k_{IViBa} (N/m)	c_{IViBa} (N s/m)	k_{IViBa} (N/m)	c_{IViBa} (N s/m)
0	0.75	–	–	745.17	21.02
0.25	0.50	501.96	8.52	–	–
0.50	0.25	385.74	4.92	–	–
0	1.00	–	–	27.45	79.97
0.25	0.75	888.96	35.15	–	–
0.75	0.25	550.92	9.06	–	–
0.50	0.50	684.74	15.30	–	–

Table 6
Optimal parameters for IViBa$_c$ and IViBa$_d$ (parallel inerter-dashpot configurations) for total mass ratios ($\mu + \gamma$) of 0.75 and 1.00.

γ	μ	IViBa$_c$		IViBa$_d$	
		k_{IViBa} (N/m)	c_{IViBa} (N s/m)	k_{IViBa} (N/m)	c_{IViBa} (N s/m)
0	0.75	–	–	1258.51	1.96
0.25	0.50	620.91	1.72	–	–
0.50	0.25	438.55	1.69	–	–
0	1.00	–	–	8.69×10^{12}	2.10
0.25	0.75	2006.10	2.44	–	–
0.75	0.25	660.87	2.31	–	–
0.50	0.50	942.51	2.33	–	–

secondary mass. Similarly, IViBa$_c$ and IViBa$_d$ exhibit a comparable parallel inerter-dashpot arrangement, with the secondary mass included only in IViBa$_c$. To isolate and quantify the influence of m_{IViBa}, this section compares the structural responses obtained using IViBa$_a$ versus IViBa$_b$, and IViBa$_c$ versus IViBa$_d$.

Figs. 6(a) and 6(b) show the structural frequency responses when the structure is equipped with IViBa$_a$ and IViBa$_b$, and with IViBa$_c$ and IViBa$_d$, respectively. The structural parameters, together with those defining the compliant soil layer and the SSI and SSSI effects, are provided in Table 2. The optimal parameters for IViBa$_a$ and IViBa$_b$, and for IViBa$_c$ and IViBa$_d$, are listed in Tables 5 and 6, respectively. For a fair comparison, the total mass ratio ($\mu+\gamma$) is kept constant. This means that for IViBa$_b$ and IViBa$_d$, which have no secondary mass ($m_{IViBa} = 0$), a configuration with $\mu = 0.75$ is made comparable to IViBa$_a$ and IViBa$_c$ configurations having $\gamma = 0.25$ and $\mu = 0.5$, or $\gamma = 0.5$ and $\mu = 0.25$. In this study, total mass ratios of 0.75 and 1.0 are considered.

As shown in Figs. 6(a) and 6(b), increasing the total mass ratio reduces the structural response at resonance. For a fixed total mass ratio, configurations with a larger inertance achieve a lower peak response. However, Tables 5 and 6 show that higher inertance values require substantially larger stiffness and damping. In particular, for IViBa$_d$ with $\mu \approx 1$, the required stiffness becomes unrealistically large. It should be highlighted that for IViBa$_c$ with a total mass ratio of 1, the case $\mu = 1$ cannot produce two equal peaks because this inertance ratio exceeds the optimal value μ_{opt}. Therefore, in the simulations, μ is set to $\mu_{opt} = 0.97$.

Overall, IViBa systems with the same total mass ratio achieve comparable levels of response reduction. Although configurations with smaller inertance benefit from lower required stiffness and damping, they exhibit substantially larger internal displacements, as shown in Figs. 6(c) and 6(d). This finding confirms that the inerter can effectively replace the secondary mass while simultaneously reducing internal motion. As a result, the device requires less physical mass and less space for its movement.

Another notable observation is that increasing the secondary mass leads to a higher optimal total mass ratio. As illustrated in Fig. 5, when $\gamma = 0.5$, the optimal total mass ratio reaches 1.32 for IViBa$_a$ and 1.38 for IViBa$_c$, compared with 1.15 and 1.17 for the case $\gamma = 0.25$. This increase is beneficial for the overall structural performance, as a larger

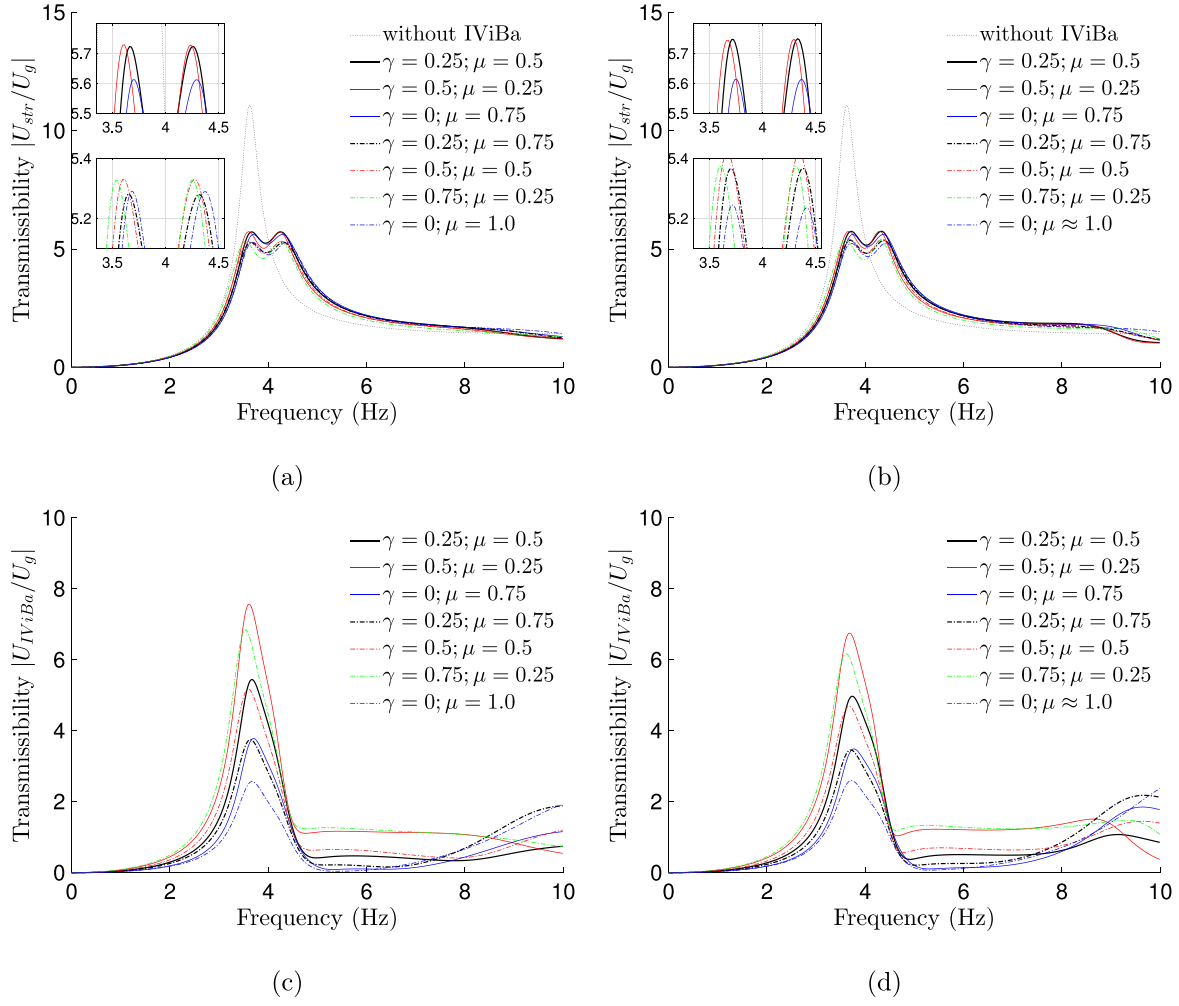


Fig. 6. Performance comparison between IViBa_a and IViBa_b (a, c), and between IViBa_c and IViBa_d (b, d).

total mass ratio generally results in further reduction of the structural response. Nevertheless, since one of the key motivations for employing inerters is to minimise the required physical mass, it is important to carefully balance the selected secondary mass and the inertance values.

4. H_2 optimisation for seismic ground motion

Optimisation for H_2 criteria is conducted to consider the effects of a wide range of frequency components on strong ground motion in this section. The equations of motion for the IViBa system introduced in Eqs. (1) and (4) can be rewritten in the state-space form,

$$\begin{aligned} \dot{x}(t) &= \boldsymbol{A}\boldsymbol{x}(t) + \boldsymbol{E}w(t), \\ u_{str}(t) &= \boldsymbol{D}\boldsymbol{x}(t), \end{aligned} \tag{7}$$

where $x(t)$ is the state vector consisting of the displacements and velocities of all degrees of freedom as well as those of the ground; $w(t)$ is the zero-mean Gaussian white noise process. By generalizing the subscript indices to $i, j \in \{a, b; c, d\}$ to represent the respective layouts given in Eqs. (1) and (4), the system matrix $\boldsymbol{A}$, the input matrix $\boldsymbol{E}$, and the output selection matrix $\boldsymbol{D}$ to the targeted structural response $u_{str}(t)$ are defined as:

$$\boldsymbol{A} = \begin{bmatrix} \boldsymbol{A}_s & \boldsymbol{E}_s\boldsymbol{C}_q \\ \boldsymbol{O}_{(n-1)\times 2n} & \boldsymbol{A}_q \end{bmatrix}, \boldsymbol{E} = \begin{bmatrix} \boldsymbol{O}_{2n\times 1} \\ \boldsymbol{E}_q \end{bmatrix}, \boldsymbol{D} = \begin{bmatrix} \boldsymbol{D}_s \\ \boldsymbol{O}_{2\times(n-1)} \end{bmatrix} \tag{8}$$

$$\boldsymbol{A}_s = \begin{bmatrix} \boldsymbol{O}_{n\times n} & \boldsymbol{I}_{n\times n} \\ -M_{i,j}^{-1}K_{i,j} & -M_{i,j}^{-1}C_{i,j} \end{bmatrix}, \boldsymbol{E}_s = \begin{bmatrix} \boldsymbol{O}_{n\times 1} \\ -\boldsymbol{R} \end{bmatrix}, \boldsymbol{D}_s = \begin{bmatrix} [\boldsymbol{T}, \boldsymbol{O}_{1\times n}] \\ [\boldsymbol{O}_{1\times n}, \boldsymbol{T}]\boldsymbol{A}_s \end{bmatrix}$$

$$\boldsymbol{A}_q = \begin{bmatrix} 0 & 1 & 0 & 0 \\ -{\omega_g}^2 & -2\zeta_g\omega_g & 0 & 0 \\ 0 & 0 & 0 & 1 \\ -{\omega_g}^2 & -2\zeta_g\omega_g & -{\omega_f}^2 & -2\zeta_f\omega_f \end{bmatrix}, \boldsymbol{E}_q = \begin{bmatrix} 0 \\ 1 \\ 0 \\ 0 \end{bmatrix}, \boldsymbol{R} = \begin{bmatrix} 1 \\ 1 \\ 1 \\ 1 \\ 0 \end{bmatrix}$$

$$\boldsymbol{C}_q = \sqrt{2\pi S_0}\begin{bmatrix} -{\omega_g}^2 & -2\zeta_g\omega_g & -{\omega_f}^2 & -2\zeta_f\omega_f \end{bmatrix}, \boldsymbol{T} = \begin{bmatrix} 0 & 1 & 0 & 0 & 0 \end{bmatrix}$$

where $n = 5$ is the number of degrees of freedom; $\boldsymbol{I}$ and $\boldsymbol{O}$ are the identity and zero matrices of appropriate dimensions; other variables in matrices $\boldsymbol{C}_q$ and $\boldsymbol{A}_q$ are defined in Eqs. (9)

A numerical optimisation is run to obtain the optimal design parameters. The well-known Power Spectral Density (PSD) model proposed by Kanai and Tajimi (K-T) with a high-pass filter [58,59,61] (hereafter referred to as the K-T spectrum) was chosen to represent the stochastic seismic excitation and is expressed as follows:

$$G_x(\omega) = S_0 \frac{\omega_g^4 + 4\zeta_g^2\omega_g^2\omega^2}{(\omega_g^2 - \omega^2)^2 + 4\zeta_g^2\omega_g^2\omega^2} \frac{\omega^4}{(\omega_f^2 - \omega^2)^2 + 4\zeta_f^2\omega_f^2\omega^2}, \tag{9}$$

where S_0, ω_g, and ζ_g are the constants determined by the amplitude of the power spectral density of the excitation, characteristic ground frequency, and damping ratio, respectively. The parameters ω_f and ζ_f denote the natural frequency and damping ratio of the second filter layer. H_2 norm of u_{str} can be obtained as

$$\sigma^2 = \boldsymbol{D}\boldsymbol{P}\boldsymbol{D}^T, \tag{10}$$

Table 7
The information of the considered Chi-Chi Taiwan ground motion records [62].

Type	Name	Station	Deterioration level		
			Fault distance (km)	Initial PGA (g)	PGA/PGV (s)
Far-field	FF-1	ILA007W	81.65	0.061	0.176
	FF-2	ILA066N	107.80	0.075	0.196
	FF-3	TAP095N	67.44	0.093	0.162
Near-field no pulse	NF-1	CHY034W	14.82	0.247	0.143
	NF-2	ICU067N	0.62	0.314	0.164
	NF-3	TCU072E	0.00	0.477	0.154
Near-field pulse-like	NF-p1	TCU051E	6.34	0.160	0.234
	NF-p2	TCU054E	7.64	0.136	0.343
	NF-p3	TCU055N	5.28	0.202	0.321

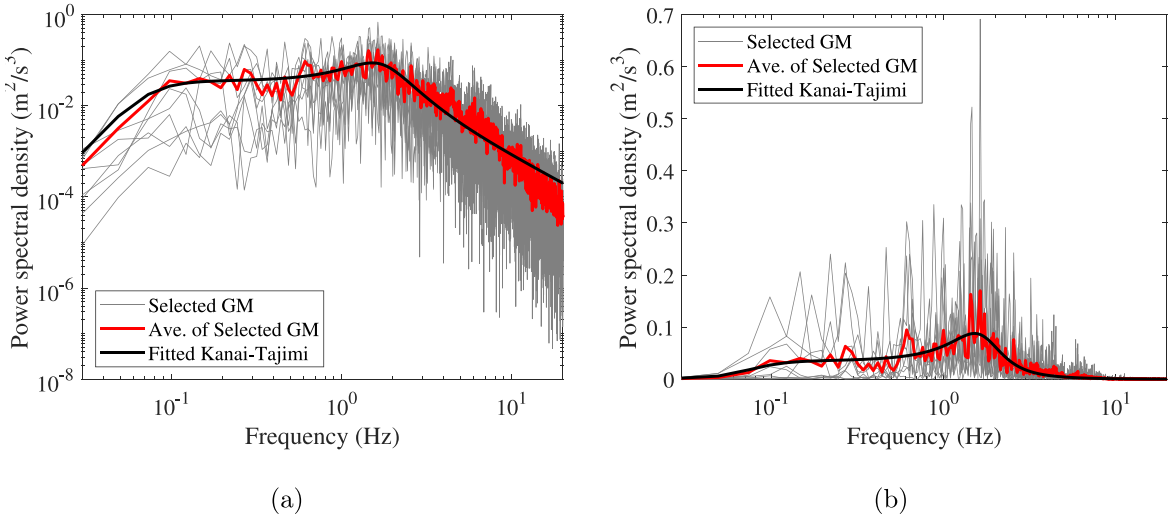


Fig. 7. Comparison of PSD characteristics of selected ground motions: (a) logarithmic scale; (b) linear scale. Here, GM denotes ground motions. (For interpretation of the references to colour in this figure legend, the reader is referred to the web version of this article.)

where $\boldsymbol{P}$ is the solution of Lyapunov equation:

$$\boldsymbol{AP} + \boldsymbol{PA}^T + \boldsymbol{EE}^T = 0. \tag{11}$$

Therefore, the optimisation problem is stated:

$$\begin{aligned} &\text{Find:} \quad b, k_{IViBa}, c_{IViBa} \\ &\text{To minimise:} \quad \sigma^2 \end{aligned} \tag{12}$$

Consistent with the H_∞ optimisation framework, the inertance, stiffness, and damping parameters are simultaneously treated as optimisation variables. The H_2-based optimisation is formulated using the K-T spectrum to evaluate IViBa performance in terms of the overall energy content of ground motions, thereby complementing the peak-response-oriented H_∞ analysis.

5. Performance assessment under various types of earthquakes

This section evaluates and compares the seismic performance of structures protected by four distinct IViBa systems. The benchmark structural model introduced in the previous section is employed in time-domain simulations subjected to nine recorded ground motions representing three earthquake categories, namely Far-field, Near-field no pulse and Near-field pulse-like as given in Table 7. It should be noted that the limited number of selected ground motions is intentional and is adopted solely to provide representative examples for verifying and illustrating the response trends obtained from the H_∞ optimisation, rather than to draw statistically generalised conclusions regarding seismic performance.

A scaled peak ground acceleration (PGA) of 0.2 g is selected to represent frequent earthquakes. The PSD characteristics of the selected ground motions are presented in Fig. 7. The grey curves represent the PSDs of individual selected ground motions, the red curve denotes their ensemble average, and the black curve shows the fitted K-T spectrum using Eq. (9). By setting $S_0 = 0.0056\ \text{m}^2/\text{s}^3$, $\omega_g = 10.82$ rad/s, $\zeta_g = 0.43$, $\omega_f = 0.46$ rad/s and $\zeta_f = 0.70$, the K-T spectrum accurately captures the frequency content of the nine ground motions, as shown in Fig. 7. Fig. 7(a) presents the PSD on a logarithmic scale over a broad frequency range, highlighting the overall spectral shape and decay, while Fig. 7(b) shows the same data on a linear scale, emphasising peak frequencies and energy concentration in the mid-frequency band. The H_∞ and H_2 optimisation methods presented in the previous sections are first employed to determine the optimal parameters of the four IViBa configurations. To further extend the analysis, a time-domain optimisation approach based on the SaDE algorithm is introduced. This enables a consistent and direct comparison of system performance using parameters obtained from fundamentally different optimisation frameworks.

The objective chosen was to find the optimum values of b, k_{IViBa} and c_IViBa that gives minimum average root-mean-square (RMS) value of the top displacement response for all considered ground motions. This condition can be expressed as:

$$\min \frac{1}{N_e} \sum_{\ell=1}^{N_e} \text{RMS}\left(x_\ell(t)\right) \tag{13}$$

where N_e is the number of ground motions. Note that the upper and lower limits of the parameter values for inertance, stiffness and damping must be set to realistic values. In this study, the limits are selected to be $0 \le b \le 2$, $0 \le k_{IViBa} \le 10^4$ and $0 \le c_{IViBa} \le 200$ (unit in N, m and s). The secondary mass ratio is fixed at 0, 0.25 and

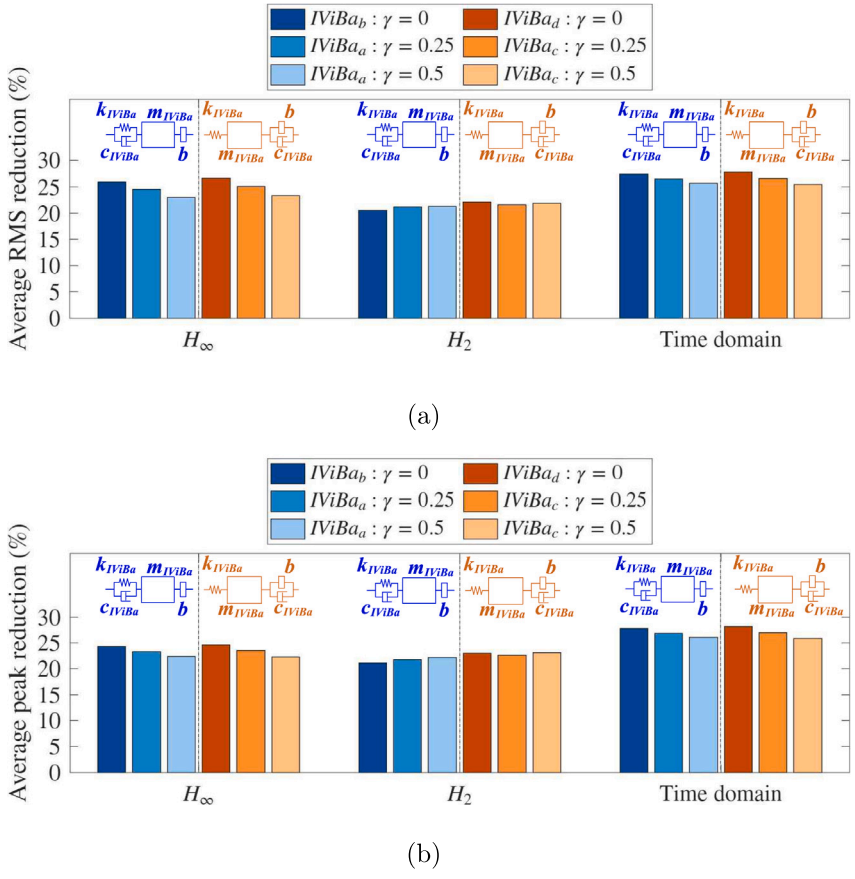


Fig. 8. Comparison of optimisation methods: (a) RMS response; (b) Peak response.

0.5, where 0.5 is adopted as the maximum value to reflect practical constraints, as larger secondary masses would necessitate significantly greater installation space and soil excavation.

The SaDE algorithm is adopted owing to its strong global search capability and self-adaptive parameter tuning, which enhance convergence performance in complex optimisation landscapes. In the present work, SaDE is initially applied to solve the H_∞ optimisation problem, thereby providing a benchmark within the frequency-domain framework. It is then further employed for direct time-domain optimisation, where performance indices are defined based on response reduction metrics. This unified use of SaDE ensures methodological consistency while allowing the influence of the optimisation domain (frequency vs. time) to be explicitly assessed.

The optimal parameters obtained from the three optimisation methods are summarised in Table 8. The results are consistent with the observations discussed in Section 3, where the H_∞ optimisation for IViBa_c and IViBa_d leads to very high stiffness values, reaching the imposed upper bound of 10^4 N/m. In contrast, the H_2 optimisation does not result in excessively large stiffness values.

Although the H_2 approach is intended to capture the characteristics of earthquake ground motions, however, it does not yield improved performance compared to the H_∞ results. Figs. 8(a) and 8(b) present the average RMS and peak response reductions, respectively, achieved by the three optimisation methods. Each bar represents the average reduction in structural response obtained with the IViBa system relative to the uncontrolled case, based on the nine ground motion records. The representative structural time-domain responses are given in Fig. 9(a)–(f). As can be seen, the H_2 approach yields the lowest performance, with an average response reduction of approximately 22%. This is followed by the H_∞ and time-domain optimisation methods, which

Table 8
Optimal parameters for different optimisation methods and configurations.

Optimisation method	Configurations	Optimal parameters		
		μ	k_{IViBa} (N/m)	c_{IViBa}(N s/m)
$\gamma = 0$				
H_∞	IViBa_b	1.002	10.72	81.83
	IViBa_d	0.93	10 000.00	2.58
H_2	IViBa_b	0.56	232.75	2.69
	IViBa_d	0.86	555.41	2.64
Time domain	IViBa_b	1.26	0.00	102.76
	IViBa_d	1.13	10 000.00	2.98
$\gamma = 0.25$				
H_∞	IViBa_a	0.905	470.34	77.8
	IViBa_c	0.89	10 000.00	2.75
H_2	IViBa_a	0.38	227.90	2.64
	IViBa_c	0.50	332.34	1.90
Time domain	IViBa_a	1.24	84.89	92.74
	IViBa_c	1.12	10 000.00	3.45
$\gamma = 0.5$				
H_∞	IViBa_a	0.82	631.17	76.17
	IViBa_c	0.83	10 000.00	3.10
H_2	IViBa_a	0.20	232.08	2.76
	IViBa_c	0.25	288.58	1.97
Time domain	IViBa_a	1.22	98.52	86.29
	IViBa_c	1.12	10 000.00	3.97

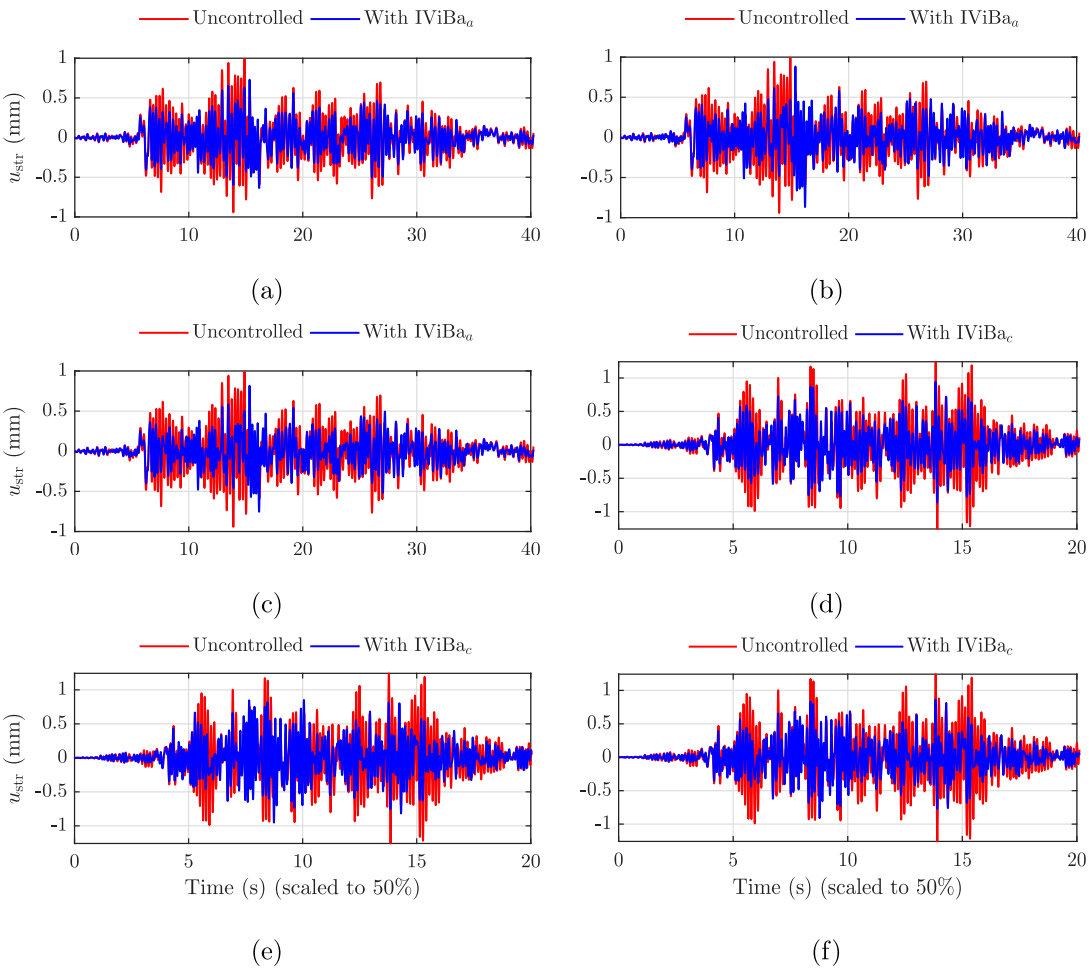


Fig. 9. Representative structural time-domain responses without and with IViBa for $\gamma = 0.25$. (a)–(c) correspond to the structure equipped with IViBa$_a$, optimised using H_∞, H_2, and Time domain optimisations, respectively, under NF-p3 ground motion. (d)–(f) show the structure with IViBa$_c$, optimised using the same criteria, under NF-p1 ground motion. Optimal parameters of the IViBa are listed in Table 8.

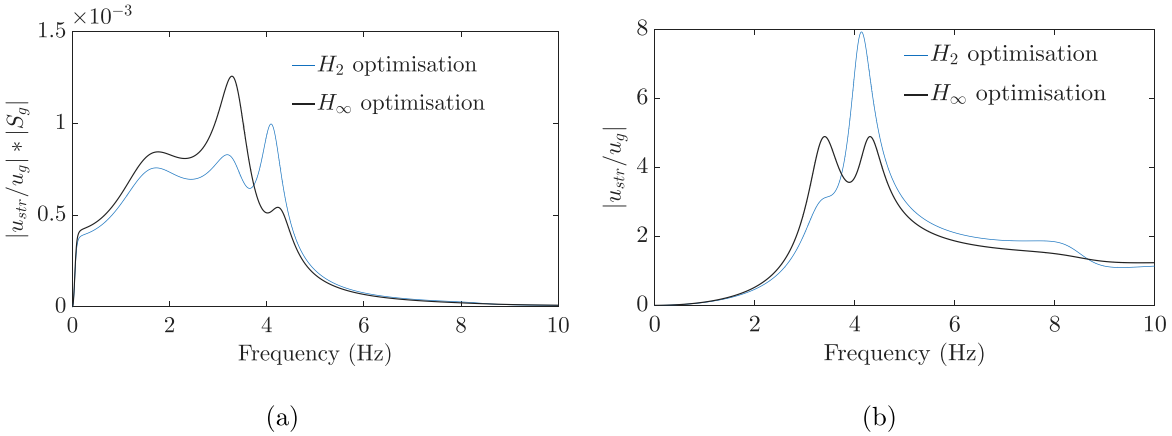


Fig. 10. Transmissibility under different optimisation criteria (a) H_2 norms with K-T spectrum (b) H_∞ norms without K-T spectrum.

achieve around 24% and 27% response reduction, respectively, for both RMS and peak responses.

The reason why the H_2 approach does not yield better performance, despite accounting for ground motion characteristics through the K-T spectrum, is attributed to the pronounced peak in the frequency response around 4 Hz, as shown in Fig. 10(a). This peak coincides with the natural frequency of the SDOF structure with compliant soil (3.6 Hz), leading to amplified response and reduced effectiveness.

Furthermore, the H_2 approach does not result in excessively large stiffness values. This is because H_2 optimisation focuses on minimising the overall energy of the system response, rather than suppressing peak amplification. As a result, it does not strongly penalise local resonance peaks, such as the one observed around 4 Hz, and therefore does

not drive the stiffness to high values to enforce a strict equal-peak condition, as illustrated in Fig. 10(b).

Assessing the performance of the four IViBa configurations in reducing both RMS and peak structural responses (Figs. 8(a) and 8(b)), the configurations without the secondary mass (IViBa$_b$ and IViBa$_d$) tend to deliver better average performance for the selected records across all three optimisation methods. The only exception is the H_2 optimisation, where IViBa$_b$ exhibits a marginally lower response reduction. These results suggest that the inerter can effectively substitute for the secondary mass, thereby reducing mass requirements while maintaining, or even enhancing, the overall performance of the IViBa systems.

6. Conclusions

This study has presented a systematic investigation of IViBa systems for seismic protection, introducing three alternative configurations – IViBa$_b$, IViBa$_c$, and IViBa$_d$ – in addition to the reference IViBa$_a$ system previously reported in the literature. The study demonstrates that IViBa systems exhibit dynamic behaviour and optimisation requirements that differ fundamentally from those of inerter-based dampers directly installed within structures.

A key outcome of the H_∞ optimisation is the identification of an optimal inertance for IViBa systems, beyond which further increases do not enhance, and may even reduce, vibration mitigation performance. This finding contrasts with conventional inerter-based control devices and underscores the necessity of explicitly optimising inertance when inerters are deployed as ground-installed vibrating barriers. The results further show that inertance cannot be treated independently, but must be considered in conjunction with stiffness and damping parameters.

The influence of dashpot placement and secondary mass inclusion was examined in detail, revealing clear performance trade-offs. Configurations employing a parallel inerter-dashpot arrangement achieve comparable or slightly improved response reduction with substantially lower damping demand. Configurations with a parallel inerter–dashpot arrangement are capable of achieving a similar level of performance to those with a parallel spring–dashpot arrangement, while requiring significantly lower damping. In the case considered, the reduction in damping demand reaches approximately 96%.

In the configuration with parallel inerter-dashpot, stiffness demands may become impractically large near the optimum. However, the results indicate that for inertance values below this threshold, physically meaningful and practically attainable parameter combinations can still be achieved. In contrast, parallel spring-dashpot configurations offer more moderate stiffness requirements across a wider inertance range, but require higher damping capacity. The inclusion of a secondary mass was shown to enhance response reduction by increasing the optimal total mass ratio, although this benefit must be balanced against the objective of minimising physical mass, which is a primary motivation for the use of inerters.

The effectiveness of the proposed IViBa configurations was further assessed through H_2 optimisation and time-domain simulations using a limited set of recorded far-field, near-field, and pulse-like earthquake ground motions. Across all cases, the IViBa systems achieved meaningful reductions in both RMS and peak structural response. Depending on the optimisation method, the average response reduction is approximately 22%–27% for the considered ground motions.

Overall, the results of this study confirm the viability of inerter-based vibrating barriers as effective, non-invasive seismic protection devices and provide practical guidance on inertance tuning, dashpot placement, and secondary mass selection. The findings establish a clear framework for informed IViBa design and offer a robust foundation for future work, including experimental validation, large-scale implementation, and the development of refined dynamic models that explicitly account for the installation location of the control system and its influence on seismic performance.

CRediT authorship contribution statement

Predaricka Deastra: Writing – original draft, Validation, Software, Methodology, Investigation, Funding acquisition, Formal analysis, Conceptualization. **Hakan Dogan:** Writing – original draft, Software, Investigation, Formal analysis. **Ruihong Xie:** Software, Formal analysis. **Marco Domaneschi:** Writing – review & editing, Supervision, Funding acquisition.

Declaration of competing interest

The authors declare that they have no known competing financial interests or personal relationships that could have appeared to influence the work reported in this paper.

Acknowledgements

This project has received funding from the European Unions Horizon Europe research and innovation programme under the Marie Skłodowska-Curie grant agreement No. 101153525. Views and opinions expressed are however those of the authors only and do not necessarily reflect those of the European Union. Neither the European Union nor the granting authority can be held responsible for them. For the purpose of open access, the authors have applied a Creative Commons Attribution (CC-BY) license to any Author Accepted Manuscript version arising from this submission.

Data availability

Data will be made available on request.

References

[1] Smith MC. Synthesis of mechanical networks: the inerter. IEEE Trans Autom Control 2002;47(10):1648–62. http://dx.doi.org/10.1109/TAC.2002.803532.

[2] Watanabe Y, Ikago K, Inoue N, Kida H, Nakaminami S, Tanaka H, Sugimura Y, Saito K. Full-scale dynamic tests and analytical verification of a force-restricted tuned viscous mass damper. In: Proceedings of the 15th world conference on earthquake engineering. Lisbon/Portugal; 2012, ID1206.

[3] Papageorgiou C, Houghton NE, Smith MC. Experimental testing and analysis of inerter devices. J Dyn Syst Meas Control 2009;131:011001. http://dx.doi.org/10.1115/1.3023120.

[4] Wang FC, Hong MF, Lin TC. Designing and testing a hydraulic inerter. Proc Inst Mech Eng C 2011;225(1):66–72. http://dx.doi.org/10.1243/09544062JMES2199.

[5] Swift SJ, Smith MC, Glover AR, Papageorgiou C, Gartner B, Houghton NE. Design and modelling of a fluid inerter. Internat J Control 2013;86(11):2035–51. http://dx.doi.org/10.1080/00207179.2013.842263.

[6] Ikago K, Saito K, Inoue N. Seismic control of single-degree-of-freedom structure using tuned viscous mass damper. Earthq Eng Struct Dyn 2012;41(3):453–74. http://dx.doi.org/10.1002/eqe.1138.

[7] Deastra P, Wagg DJ, Sims ND, Mills RS. Experimental shake table validation of damping behaviour in inerter-based dampers. Bull Earthq Eng 2023;21(3):1389–409. http://dx.doi.org/10.1007/s10518-022-01376-1.

[8] Wagg, David J. A review of the mechanical inerter: historical context, physical realisations and nonlinear applications. Nonlinear Dynam 2021;104(1):13–34. http://dx.doi.org/10.1007/s11071-021-06303-8.

[9] Sugimura Y, Goto W, Tanizawa H, Saito K, Ninomiya T, Nagasaku T. Response control effect of steel building structure using tuned viscous mass damper. In: Proceedings of the 15th world conference on earthquake engineering. Lisbon/Portugal; 2012, ID0138.

[10] Nakaminami S, Kida H, Ikago K, Inoue N. Dynamic testing of a full-scale hydraulic inerter-damper for the seismic protection of civil structures. In: 7th international conference on advances in experimental structural engineering. AESE 2017, Eucentre; p. 41–54.

[11] Ikago K, Sugimura Y, Saito K, Inoue N. Seismic displacement control of multiple-degree-of-freedom structures using tuned viscous mass dampers. In: Proceedings of the 8th international conference on structural dynamics. EURODYN, Leuven/Belgium; 2011, p. 3.

[12] Giaralis A, Petrini F. Wind-induced vibration mitigation in tall buildings using the tuned mass-damper-inerter. J Struct Eng 2017;143(9):04017127. http://dx.doi.org/10.1061/(ASCE)ST.1943-541X.0001863.

[13] Lei Z, Liu G, Li W, Yang Q, Wen M, Li H. Vibration suppression and performance enhancement of a pendulum tuned mass damper-inerter with geometrical nonlinearity for wind turbine towers: Z. Lei and et al. Nonlinear Dyn 2026;114(9):653. http://dx.doi.org/10.1007/s11071-026-12534-4.

[14] Lei Z, Liu G, Li W, Yang Q, Zhang J, Li H, Qiu Z. Dynamical modelling and vibration dissipation of monopiles for offshore wind turbine with multiple prestressed tuned mass dampers under multi-hazard excitations. Ocean Eng 2026;351:124349. http://dx.doi.org/10.1016/j.oceaneng.2026.124349.

[15] Lei Z, Liu G, Wang H, Li M, Zhou L, Wang T. Vibration control of wind turbine towers with the nonlinear tuned liquid damper considering the aero-elastic coupling behavior. Commun Nonlinear Sci Numer Simul 2025;109306.

[16] Zhang R, Zhao Z, Dai K. Seismic response mitigation of a wind turbine tower using a tuned parallel inerter mass system. Eng Struct 2019;180:29–39. http://dx.doi.org/10.1016/j.engstruct.2018.11.020.

[17] Li Y, Jiang JZ, Neild SA, Wang H. Optimal inerter-based shock–strut configurations for landing-gear touchdown performance. J Aircraft 2017;54(5):1901–9. http://dx.doi.org/10.2514/1.C034276.

[18] Li Y, Jiang JZ, Sartor P, Neild SA, Wang H. Including inerters in aircraft landing gear shock strut to improve the touch-down performance. Procedia Eng 2017;199:1689–94. http://dx.doi.org/10.1016/j.proeng.2017.09.366.

[19] Dong X, Liu Y, Chen MZ. Application of inerter to aircraft landing gear suspension. In: 2015 34th Chinese control conference. CCC, IEEE; p. 2066–71. http://dx.doi.org/10.1109/ChiCC.2015.7259953.

[20] Dogan H, Sims ND, Wagg DJ. Implementation of inerter-based dynamic vibration absorber for chatter suppression. J Manuf Sci Eng 2023;145(8):084502. http://dx.doi.org/10.1115/1.4062118.

[21] Dogan H, Ozsoy M, Ozturk E, Wagg DJ, Sims ND. Analysis of virtual inerter-based passive absorber for active chatter control. J Sound Vib 2024;578:118359. http://dx.doi.org/10.1016/j.jsv.2024.118359.

[22] Lewis TD, Jiang JZ, Neild SA, Gong C, Iwnicki SD. Using an inerter-based suspension to improve both passenger comfort and track wear in railway vehicles. Veh Syst Dyn 2020;58(3):472–93. http://dx.doi.org/10.1080/00423114.2019.1589535.

[23] Jiang JZ, Matamoros-Sanchez AZ, Goodall RM, Smith MC. Passive suspensions incorporating inerters for railway vehicles. Veh Syst Dyn 2012;50(sup1):263–76. http://dx.doi.org/10.1080/00423114.2012.665166.

[24] Zhang X, Li H, Cheng J, Sheng L, Yao Y. Adaptive stability mechanism of high-speed train employing parallel inerter yaw damper. Veh Syst Dyn 2023;61(1):38–57. http://dx.doi.org/10.1080/00423114.2022.2045027.

[25] Deastra P, Dogan H, Xie R, Ikago K. Shake table experimental validation of auxiliary mass effects in a tuned viscous mass damper. Structures 2025;80:109681. http://dx.doi.org/10.1016/j.istruc.2025.109681.

[26] Lazar IF, Neild SA, Wagg DJ. Using an inerter-based device for structural vibration suppression. Earthq Eng Struct Dyn 2014;43(8):1129–47. http://dx.doi.org/10.1002/eqe.2390.

[27] Marian Laurentiu, Giaralis Agathoklis. Optimal design of a novel tuned mass-damper-inerter (TMDI) passive vibration control configuration for stochastically support-excited structural systems. Probabilistic Eng Mech 2014;38:156–64. http://dx.doi.org/10.1016/j.probengmech.2014.03.007.

[28] Hu Y, Chen MZ, Shu Z, Huang L. Analysis and optimisation for inerter-based isolators via fixed-point theory and algebraic solution. J Sound Vib 2015;346:17–36. http://dx.doi.org/10.1016/j.jsv.2015.02.041.

[29] Hu Y, Chen MZ. Performance evaluation for inerter-based dynamic vibration absorbers. Int J Mech Sci 2015;99:297–307. http://dx.doi.org/10.1016/j.ijmecsci.2015.06.003.

[30] Deastra P, Wagg DJ, Sims ND. Using a tuned-inerto-viscous-hysteretic-damper (TIVhD) for vibration suppression in multi-storey building structures. IOP Conf Ser: Earth Environ Sci 2021;708(1):012012. http://dx.doi.org/10.1088/1755-1315/708/1/012012.

[31] Barredo E, Blanco A, Colín J, Penagos VM, Abúndez A, Vela LG, Meza V, Cruz RH, Mayén J. Closed-form solutions for the optimal design of inerter-based dynamic vibration absorbers. Int J Mech Sci 2018;144:41–53. http://dx.doi.org/10.1016/j.ijmecsci.2018.05.025.

[32] Zeng C, Zhang Z, Su N. Multi-objective seismic mitigation of transmission towers using single-endpoint double tuned inerter dampers. Structures 79:109583. http://dx.doi.org/10.1016/j.istruc.2025.109583.

[33] Kang Jianfei, Ikago Kohju. Seismic control of multidegree-of-freedom structures using a concentratedly arranged tuned viscous mass damper. Earthq Eng Struct Dyn 2023;52(14):4708–32. http://dx.doi.org/10.1002/eqe.3977.

[34] Ikago K, Sugimura Y, Saito K, Inoue N. Modal response characteristics of a multiple-degree-of-freedom structure incorporated with tuned viscous mass dampers. J Asian Archit Build Eng 2012;11(2):375–82. http://dx.doi.org/10.3130/jaabe.11.375.

[35] Nakaminami S, Ikago K, Inoue N, Kida H. Response characteristics of a base-isolated structure incorporated with a force-restricted viscous mass damper. In: Proceedings of the 15th world conference on earthquake engineering. Lisbon/Portugal; 2012.

[36] Ogino M, Sumiyama T. Structural design of a high-rise building using tuned viscous mass dampers installed across three consecutive storeys. In: 12th international conference on computational structures technology. vol. 225, 2014, http://dx.doi.org/10.4203/ccp.106.225.

[37] Ishii M, Kazama H, Miyazaki K, Murakami K. Application of tuned viscous mass damper to super-high-rise buildings. In: Proceedings of the 6th world conference of structural control and health monitoring. Barcelona/Spain; 2014, p. 2825–33.

[38] Hao L, He H, Tan P. Response mitigation performance and energy dissipation enhancement of tuned viscous mass damper applied on adjacent structures. Soil Dyn Earthq Eng 2021;150:106902. http://dx.doi.org/10.1016/j.soildyn.2021.106902.

[39] Ji X, Jia R, Wang L, Wang M, Wu X. Seismic design and performance assessment of a retrofitted building with tuned viscous mass dampers (TVMD). Eng Struct 2024;305:117688. http://dx.doi.org/10.1016/j.engstruct.2024.117688.

[40] Deastra Predaricka, Wagg DJ, Sims ND. The effect of a tuned-inerter-damper on the seismic response of base-isolated structures. In: Proceedings of the 16th European conference on earthquake engineering. Thessaloniki/Greece; 2018.

[41] De Domenico D, Impollonia N, Ricciardi G. Soil-dependent optimum design of a new passive vibration control system combining seismic base isolation with tuned inerter damper. Soil Dyn Earthq Eng 2018;105:37–53. http://dx.doi.org/10.1016/j.soildyn.2017.11.023.

[42] De Domenico D, Ricciardi G. Improving the dynamic performance of base-isolated structures via tuned mass damper and inerter devices: A comparative study. Struct Control Health Monit 2018;25(10):e2234. http://dx.doi.org/10.1002/stc.2234.

[43] De Domenico D, Ricciardi G. An enhanced base isolation system equipped with optimal tuned mass damper inerter (TMDI). Earthq Eng Struct Dyn 2018;47(5):1169–92. http://dx.doi.org/10.1002/eqe.3011.

[44] Djerouni S, Ounis A, Elias S, Abdeddaim M, Rupakhety R. Optimization and performance assessment of tuned mass damper inerter systems for control of buildings subjected to pulse-like ground motions. Structures 2022;38:139–56. http://dx.doi.org/10.1016/j.istruc.2022.02.007.

[45] Alotta G, Biondo C, Giaralis A, Failla G. Seismic protection of land-based wind turbine towers using the tuned inerter damper. Structures 2023;51:640–56. http://dx.doi.org/10.1016/j.istruc.2023.03.004.

[46] Zhang T, Wang W, Li X. Optimization and evaluation of tuned inerter-based dampers for mitigating coupled responses of offshore wind turbines. Ocean Eng 2024;312:119146. http://dx.doi.org/10.1016/j.oceaneng.2024.119146.

[47] Elias S, Beer M. Vibration control and energy harvesting of offshore wind turbines installed with TMDI under dynamical loading. Eng Struct 2024;315:118459. http://dx.doi.org/10.1016/j.engstruct.2024.118459.

[48] Elias S, Beer M, Mahmoud H. Assessments of seismic response and energy harvesting of offshore wind turbines equipped with tuned mass damper inerter. J Struct Eng 2025;151(10):04025145. http://dx.doi.org/10.1061/JSENDH.STENG-14938.

[49] Han G, Wu Y, Hou G, Yue Z. Optimal design of nuclear power plants containment with tuned mass damper inerter device for earthquake loadings. J Mech Sci Technol 2023;37(11):5607–21. http://dx.doi.org/10.1007/s12206-023-1004-6.

[50] Zhang S, Hou G, Yang C, Yue Z, Wang Y, He M, Cai X. Investigations on seismic performance of nuclear power plants equipped with an optimal BIS-TMDI considering FSI effects. Nucl Eng Technol 2024;56(7):2595–609. http://dx.doi.org/10.1016/j.net.2024.02.019.

[51] Li Y, Li S, Tan P. A novel tuned mass damper inerter: optimal design, effectiveness comparison, and robustness investigation. Structures 2023;55:1262–76. http://dx.doi.org/10.1016/j.istruc.2023.06.076.

[52] Deastra P, Dogan H, Zhou F, Xie R, Ikago K. The role of auxiliary mass element in the dynamic performance of tuned-inerter devices. Structures 88:111778. http://dx.doi.org/10.1016/j.istruc.2026.111778.

[53] Cacciola P, Tombari A. Vibrating barrier: a novel device for the passive control of structures under ground motion. Proc R Soc A 2015;471(2179):20150075. http://dx.doi.org/10.1098/rspa.2015.0075.

[54] Tombari A, Espinosa MG, Alexander NA, Cacciola P. Vibration control of a cluster of buildings through the vibrating barrier. Mech Syst Signal Process 2018;101:219–36. http://dx.doi.org/10.1016/j.ymssp.2017.08.034.

[55] Cacciola P, Shadlou M, Ayoub A, Rashed YF, Tombari A. Exploring the performances of the vibrating barriers for the seismic protection of the Zoser pyramid. Sci Rep 2022;12(1):5542.

[56] Cacciola P, Catania N, Fiorini N, Occhipinti G, Morris P, Spina D, Tombari A. Design of novel vibrating barriers for the seismic protection of the Messina Cathedral. In: 17th world conference on earthquake engineering. 17WCEE, Sendai/Japan; 2022.

[57] Cacciola P, Tombari A, Giaralis A. An inerter-equipped vibrating barrier for noninvasive motion control of seismically excited structures. Struct Control Health Monit 2020;27(3):e2474. http://dx.doi.org/10.1002/stc.2474.

[58] K. Kanai. Semi-empirical formula for the seismic characteristics of the ground. Bull Earthq Res Inst Univ Tokyo 1957;35:309–25.

[59] Tajimi H. A statistical method of determining the maximum response of a building structure during an earthquake. In: Proc. of the 2nd world conference on earthquake engineering. Tokyo, Japan; 1960, p. 781–97.

[60] Qin AK, Suganthan PN. Self-adaptive differential evolution algorithm for numerical optimization, booktitle=2005 IEEE congress on evolutionary computation. vol. 2, p. 1785–91.

[61] Taflanidis AA, Giaralis A, Patsialis D. Multi-objective optimal design of inerter-based vibration absorbers for earthquake protection of multi-storey building structures. J Frankl Inst 2019;356(14):7754–84. http://dx.doi.org/10.1016/j.jfranklin.2019.02.022.

[62] Hu S, Hu R, Yang M, Meng D. Influence of the deteriorated anti-seismic devices on seismic performance and device behavior of continuous girder bridges. Earthq Struct 2023;24(5):333–43. http://dx.doi.org/10.12989/eas.2023.24.5.333.